Journal of Applied Physics

Understanding the signal amplification in dual-gate FET-based biosensors

Cite as: J. Appl. Phys. **128**, 184502 (2020); https://doi.org/10.1063/5.0010136
Submitted: 07 April 2020 . Accepted: 23 October 2020 . Published Online: 10 November 2020

Jae-Hyuk Ahn, Bongsik Choi, and Sung-Jin Choi

View Online
Export Citation
CrossMark

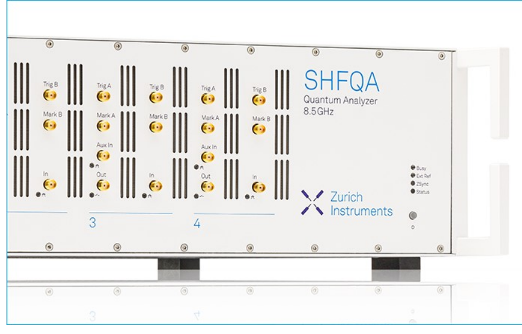

Learn how to perform
the readout of up
to 64 qubits in parallel
With the next generation
of quantum analyzers
on November 17th
Register now

© 2020 Author(s).

Journal of Applied Physics ARTICLE scitation.org/journal/jap

Understanding the signal amplification in dual-gate FET-based biosensors

Cite as: J. Appl. Phys. **128**, 184502 (2020); doi: 10.1063/5.0010136
Submitted: 7 April 2020 · Accepted: 23 October 2020 ·
Published Online: 10 November 2020

Jae-Hyuk Ahn,[1] Bongsik Choi,[2] and Sung-Jin Choi[2,a)]

AFFILIATIONS

[1]Department of Electronics Engineering, Chungnam National University, Daejeon 34134, Korea
[2]School of Electrical Engineering, Kookmin University, Seoul 02707, Korea

[a)]**Author to whom correspondence should be addressed:** sjchoiee@kookmin.ac.kr

ABSTRACT

Field-effect transistor (FET)-based sensors allow rapid, label-free electrical detection of chemical and biological species and are easy to use. Dual-gate FET-based biosensors enable sensitive detection with high intensity signal by their distinctive structure based on a combination of solid and liquid gates. However, the underlying mechanism of signal amplification to explain the experimental results has not been well explained with theoretical analysis. In this work, a theoretical approach based on device physics is used to interpret the signal enhancement in dual-gate FET-based biosensors. The analysis is verified with a simulation method for pH sensors based on a well-established commercialized semiconductor 3D technology computer-aided design simulation. The pH sensing parameters are comprehensively investigated as a function of the electrical characteristics of dual-gate FETs: the voltage, current, and normalized current signals are directly correlated with capacitive coupling, transconductance, and subthreshold swing, respectively. Our theoretical analysis provides design guidelines for sensitive dual-gate FET-based biosensors.

Published under license by AIP Publishing. https://doi.org/10.1063/5.0010136

INTRODUCTION

Field-effect transistor (FET)-based sensors have received much attention in the biomedical field due to their attractive merits. Label-free electrical detection of biomolecules with FET-based sensors allows not only fast and simple analysis without labeling processes but also high portability due to the integration of sensors with compact electrical readout circuits. The sensors are sensitive to the electrical charges of analytes, which provide a broad range of biomedical applications: pH sensing,[1–4] detection of proteins[1,5–7] and DNA,[8,9] and monitoring of cell activity.[10–12] When FET-based biosensors are fabricated in low-dimensional structures such as nanowires and nanoribbons, their high surface-to-volume ratio enhances the sensitivity with a low limit of detection.

Dual-gate FET-based biosensors have been introduced for further signal amplification by simple structural modification.[6,13–21] In addition to a sweeping (or driving) gate to measure the voltage signal, a biasing (or supporting) gate for the sensor to operate in a sensitive region is additionally integrated to make a dual-gate structure. As this dual-gate structure originated from thin-film silicon-on-insulator (SOI) FETs, the back-gate effect on SOI FETs can explain how the additional gate affects the electrical characteristics of dual-gate FET-based biosensors.[22–25] In the dual-gate structure, the voltage signal induced on the side of the biasing gate is amplified as the threshold voltage change, which is measured with the sweeping gate by the capacitive coupling between the two gates. Go *et al.* conducted a pioneering work on the analytical theory for signal amplification in dual-gate FET-based biosensors to explain experimental results.[26] They concluded that a dual-gate FET-based biosensor provides a better signal-to-noise ratio, compared to a single-gate counterpart, if the instrumentation noise is the dominant factor and defines the lower limit of the sensor performance. Although previous studies provide theoretical analyses on the signal amplification of FET-based biosensors,[27–29] a comprehensive analysis to correlate the electrical characteristics with the sensing parameters (i.e., voltage, current, and normalized current signals) of dual-gate FET-based biosensors has not been fully performed yet. In this work, we provide a systematic analysis on the sensing parameters to explain the signal amplification in dual-gate FET-based biosensors. We investigate the effects of biasing conditions and device geometry of dual-gate FETs on the sensing parameters. Our analysis is based on the physics of semiconductor devices and technology computer-aided design (TCAD)

Published under license by AIP Publishing.

TABLE I. Summary of related equations between sensing parameter and device characteristics of dual-gate FET-based biosensors.

Sensing parameter	Device characteristics	Related equation
$\Delta V_{T,BG}$	$\frac{C_{LG}}{C_{BG}}$	$\Delta V_{T,BG} = \frac{C_{LG}}{C_{BG}} \Delta V_{T,LG}$
ΔI_D	$g_{m,LG}$	$\Delta I_D = g_{m,LG} \Delta V_{T,LG}$
$\frac{\Delta I_D}{I_D}$	SS_{LG}	$\log\left(1 + \frac{\Delta I_D}{I_{D0}}\right) = \frac{\Delta V_{T,LG}}{SS_{LG}}$

simulations. The 3D TCAD simulation for FET-type pH sensors, a proof-of-concept demonstration for biosensors to detect charged biomolecules, has advantages in easy control of the geometry and biasing conditions to study the operation of biosensors.[30] We address how the electrical characteristics such as capacitive coupling, transconductance, and subthreshold slope correlate with the sensing parameters to provide design guidelines for highly sensitive biosensors, as summarized in Table I.

RESULTS AND DISCUSSION

Figure 1 shows a typical structure of dual-gate FETs. A liquid gate (or reference electrode) dipped into a buffer solution is combined with a back-gated device where a silicon nanowire or nanoribbon is implemented on the silicon-on-insulator (SOI) wafer and the bottom substrate serves as a bottom gate. Either the liquid gate or the bottom gate is used as a sweeping gate and the other is used as a biasing gate. The Si channel can be replaced with other semiconductor materials such as carbon nanotubes,[31,32] graphene,[9,33] In_2O_3 nanowires,[34] and MoS_2.[35] Note that a top-gate dielectric (i.e., SiO_2, Al_2O_3, or HfO_2) is formed on top of the silicon channel to prevent a leakage current from directly flowing through the buffer solution. At the same time, the top-gate dielectric is used as a pH-sensitive layer, leading to a change in the surface potential depending on the pH value. Both the liquid gate and bottom gate can modulate the drain current (I_D) flowing through the silicon channel from the drain to the source. The electric field generated from the bottom gate is transferred to the silicon channel through the buried oxide (BOX); thus, the electron carriers in the channel are controlled via the field effect. Similarly, the voltage applied to the liquid gate determines the electric potential of the buffer solution in contact with the top-gate dielectric, and thus the electron concentration is modulated. The simulation method for a dual-gate FET is similar to that reported in our previous study;[30] the simulation method is described in detail in the Methods section and in the supplementary material. Briefly, we set the length, width, and thickness of a p-type silicon nanowire with a doping concentration of 10^{15} cm^{-3} to 1 μm, 200 nm, and 30 nm, respectively. The device may operate in the fully depleted mode because the top silicon thickness is much smaller than the depletion width of the channel. The thicknesses of the BOX were 100, 300, and 500 nm to investigate the structural effect on the sensitivity. An ionic solution (i.e., phosphate-buffered saline, PBS) was modeled as an intrinsic semiconductor material by considering the ionic concentration and valance of the ions in the ionic solution. The values of the surface charge densities on the SiO_2 surface for each pH value were calculated using the site-binding model (SBM) to describe the electrical characteristics of the electrolyte.[2,36] The dual-gate FET exhibits typical n-type characteristics where the threshold voltage, subthreshold swing, and on–off ratio are tuned by varying the liquid-gate voltage (V_{LG}) as shown in Figs. 2(a)–2(f).

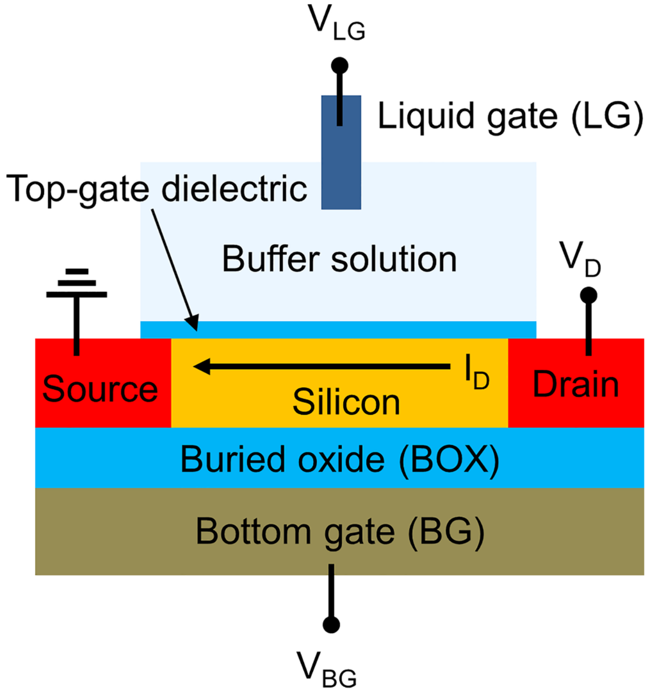

FIG. 1. Schematic of a typical dual-gate FET consisting of liquid gate and bottom gate, which control the potential of the silicon channel through buffer solution/top dielectric and buried oxide (BOX), respectively. The thicknesses of the top dielectric, top Si, and BOX are 3 nm, 30 nm, and 300 nm, respectively. The doping concentration of the p-type top Si is 10^{15} cm^{-3}.

To investigate the pH sensing performance, we observed the changes in the electrical characteristics of a dual-gate FET in buffer solutions with different pH values in the simulation. As the pH value decreases from 8 to 6, the portion of the high-current regime represented by a reddish color increases, which indicates an increase in the conductance of the dual-gate FET for the given V_{BG} and V_{LG} at a lower pH value [Figs. 2(g)–2(i)]. In a solution with a lower pH value, the higher concentration of H^+ ions in the buffer solution increases the positive charge density on the pH sensing layer (i.e., SiO_2), which attracts the electrons in the silicon channel and increases the drain current. For a quantitative analysis of the pH response affected by the operation condition of dual gates, we defined the pH responsivity (or voltage parameter) as the gate voltage (or threshold voltage) needed to restore the drain current upon a change of one pH unit, which is expressed with the unit mV/pH. To calculate the pH responsivity, we first extracted the threshold voltages for pH 6, 7, and 8 as shown in Figs. 3(a) and 3(b), and then differentiated the threshold voltages with respect to pH, where the threshold voltage (V_T) is defined as the

Published under license by AIP Publishing.

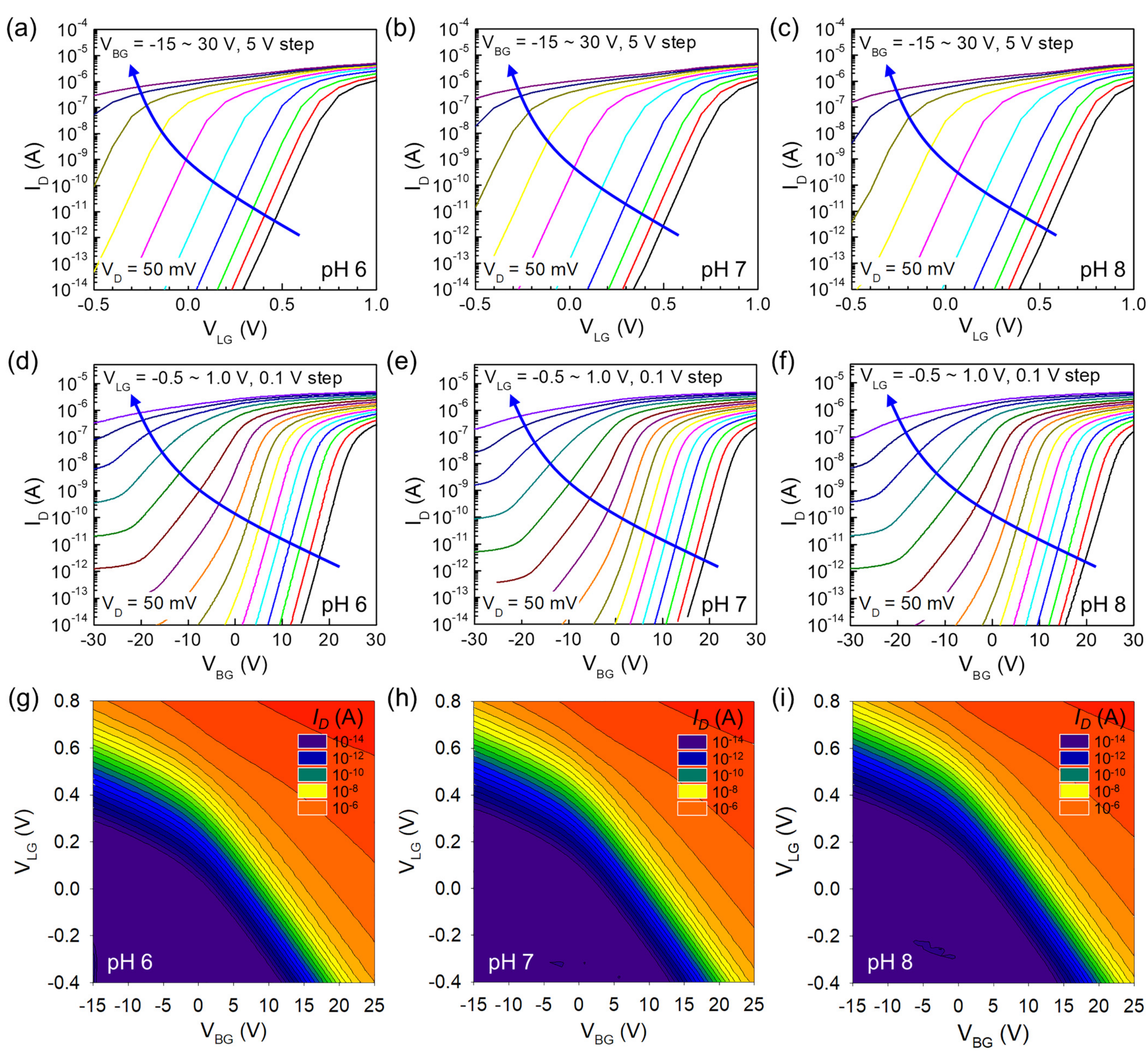

FIG. 2. Simulated drain current (I_D)–liquid-gate voltage (V_{LG}) characteristics of the dual-gate FET with buffer solutions of (a) pH 6, (b) pH 7, and (c) pH 8. The I_D–V_{LG} curve and threshold voltage are shifted by the voltage applied to the bottom gate (V_{BG}). Simulated I_D–V_{BG} characteristics of the dual-gate FET with buffer solutions of (d) pH 6, (e) pH 7, and (f) pH 8. The I_D–V_{BG} curve and threshold voltage are shifted by V_{LG}. The two-dimensional map of I_D as a function of V_{LG} and V_{BG} at (g) pH 6, (h) pH 7, and (i) pH 8. Note that the BOX thickness is 300 nm.

gate voltage required to cause the drain current of 10 nA. Because there are two gates in a dual-gate FET, the pH responsivity can be measured using either the liquid gate or the bottom gate sweeping while a constant voltage is applied to the other gate. When the liquid gate is employed as the sweeping gate to sense the pH change, the pH responsivity is slightly increased by ∼10% by the bottom-gate voltage, with a value below 60 mV/pH at room temperature, which is known as the Nernst limit [Fig. 3(c)]. A slight increase in the pH responsivity by the bottom-gate voltage was also observed for other BOX thicknesses (100 nm and 500 nm). This result is attributed to a change in the capacitive coupling between the liquid gate and channel by the bottom gate, which is discussed

Published under license by AIP Publishing.

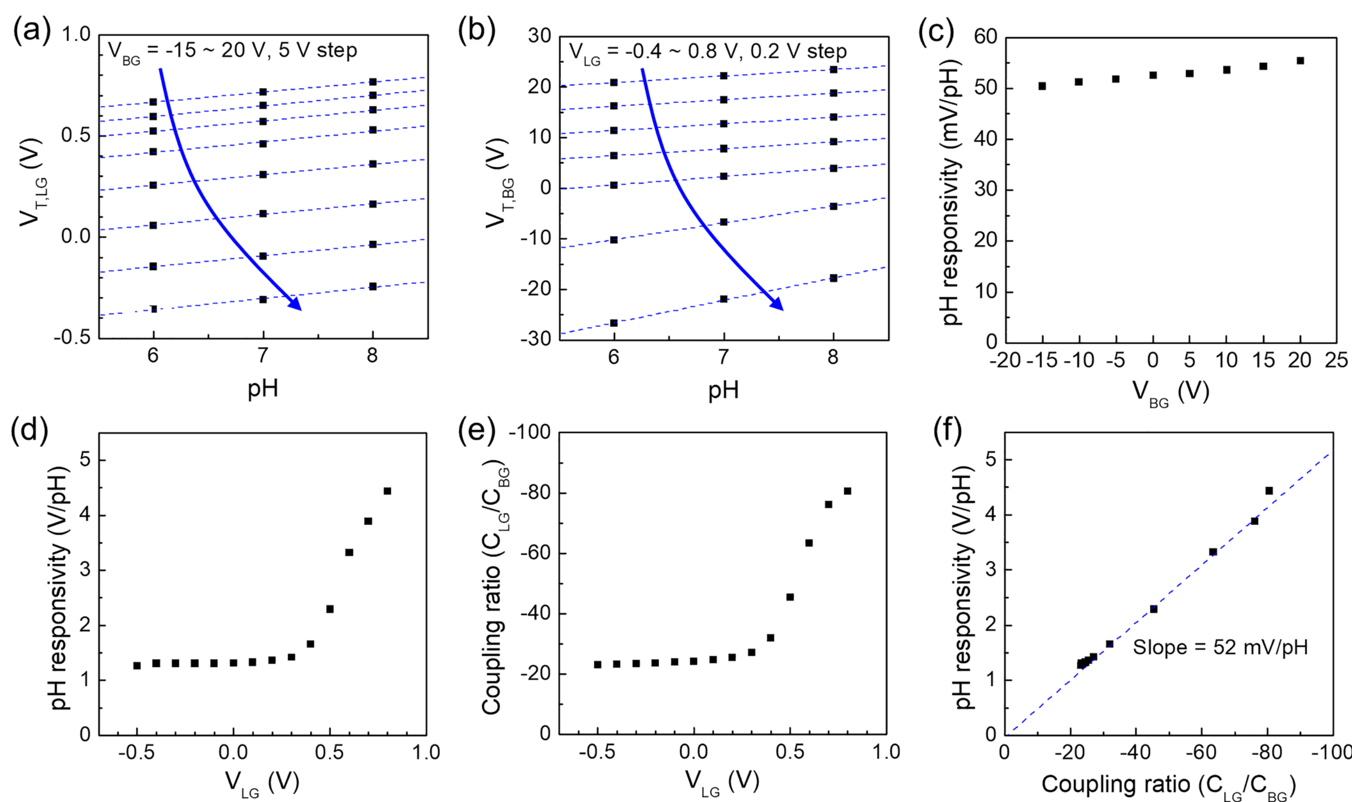

FIG. 3. (a) Threshold voltage measured by the liquid gate ($V_{T,LG}$) as a function of the pH value for various values of V_{BG}. (b) Threshold voltage measured by the bottom gate ($V_{T,BG}$) as a function of the pH value for various values of V_{LG}. The blue dashed lines shown in (a) and (b) indicate the linear regression lines for the data, where the slope is the pH responsivity with the unit mV/pH. (c) pH responsivity measured by the liquid gate as a function of V_{BG}. (d) pH responsivity measured by the bottom gate as a function of V_{LG}. (e) Capacitive coupling ratio (C_{LG}/C_{BG}) as a function of V_{LG}. (f) pH responsivity measured by the bottom gate vs C_{LG}/C_{BG}. The blue dashed line is a linear fit through the data, showing a linear relationship with a slope of 52 mV/pH. Note that the BOX thickness is 300 nm.

in detail in the supplementary material. In contrast, the pH responsivity can increase beyond the Nernst limit (60 mV/pH) when the bottom gate is utilized as the sweeping gate [Fig. 3(d)]. Moreover, the pH responsivity measured with the bottom gate improves as the liquid-gate voltage increases. This result shows that the enhanced pH responsivity beyond the Nernst limit is a distinctive feature of dual-gate FETs observed in a variety of devices composed of nanowires,[3,14] nanoribbons,[15,18,37] and nanowire–nanoplate structures.[17]

In the dual-gate FET structure, the behavior of the pH responsivity can be explained by the capacitive coupling between the liquid/bottom gates and channel because the electric potential induced by the pH solution at the liquid-gate side is capacitively coupled to the bottom gate via the channel.[6,13,14,18] When the capacitive coupling between the liquid gate and channel (C_{LG}) increases or the capacitive coupling between the bottom gate and channel (C_{BG}) decreases, the pH change at the liquid-gate side is amplified by the improved coupling ratio (C_{LG}/C_{BG}) to the voltage signal at the bottom gate. Specifically, the coupling ratio increases as the liquid voltage increases, as shown in Fig. 3(e). A high liquid voltage causes a high value of C_{LG}, i.e., capacitive coupling between the liquid and channel, by forming an electron channel close to the insulator/electrolyte interface. As shown in Figs. 3(d) and 3(e), the pH responsivity and coupling ratio simultaneously increase as the liquid-gate voltage increases. Here, the capacitive coupling ratio (C_{LG}/C_{BG}) was obtained from a slope dV_{BG}/dV_{LG} in the two-dimensional map of the drain current (I_D) as a function of V_{LG} and V_{BG} for pH 7 [Fig. 2(h)] at the threshold voltage condition ($I_D = 10$ nA). Note that Go *et al.* derived analytical equations for the capacitive coupling ratio between the liquid and bottom gates under various bias conditions,[26] which are well fitted with our TCAD results (Fig. S3 in the supplementary material). Figure 3(f) directly shows the linear relationship between the pH responsivity and capacitive coupling ratio with a slope of 52 mV/pH, which is close to the value of the pH responsivity measured with the liquid gate. The pH response at the liquid-gate side is amplified by the coupling ratio of the liquid and back gates to the high signal. Thus, the voltage signal at the back gate ($\Delta V_{T,BG}$) can be written as $\Delta V_{T,BG} = (C_{LG}/C_{BG}) \cdot \Delta V_{T,LG}$, where $\Delta V_{T,LG}$ is the pH-induced change in the potential at the liquid-gate side (Table I). This pH

Published under license by AIP Publishing.

responsivity can be easily controlled by the capacitive coupling ratio (C_{LG}/C_{BG}), which is a function of the biasing condition and geometry.

Figure 4(a) shows the two-dimensional map of the current change (ΔI_D) after the pH value increases from 6 to 8. The potential change caused by the pH change at the liquid-gate side is transduced to the current signal through the field effect. Because the pH-induced potential can be equivalently considered the liquid-gate voltage, it is inferred that the current change due to the pH change increases when the drain current is significantly modulated by the liquid-gate voltage. To verify this hypothesis, we obtained the transconductance ($g_{m,LG} = dI_D/dV_{LG}$), representing how much the drain current is modulated by the liquid-gate voltage, and compared it with the current change (ΔI_D). The two-dimensional map of the transconductance ($g_{m,LG}$) shown in Fig. 4(b) has a similar contour and shape as that of the current change (ΔI_D) shown in Fig. 4(a). The plot of the current change as a function of the transconductance shown in Fig. 4(c) was obtained from the pairs ($g_{m,LG}$, ΔI_D) where $g_{m,LG}$ and ΔI_D are the values at each of (V_{LG}, V_{BG}) in Figs. 4(a) and 4(b), respectively. Figure 4(c) shows the linear dependence between the transconductance and current change. The current change shows a maximum value when the transconductance is also maximized. Because high mobility leads to high transconductance, it is expected that a high-current signal from the dual-gate FETs can be obtained with mobility engineering or the selection of high mobility channel materials.[38] The slope of 107 mV between the transconductance and current change is similar to the value calculated from the pH responsivity in Fig. 3(f) and the pH difference as $52\,\text{mV/pH} \times \text{pH}\ 2 = 104\,\text{mV}$. This result indicates that the current change induced by the pH difference is also correlated with the pH response at the insulator/electrolyte interface. From the results in Fig. 4(c), the current signal (ΔI_D) can be written as $\Delta I_D = g_{m,LG}\,\Delta V_{T,LG}$, where $\Delta V_{T,LG}$ is the pH-induced change in the potential at the liquid-gate side (Table I).

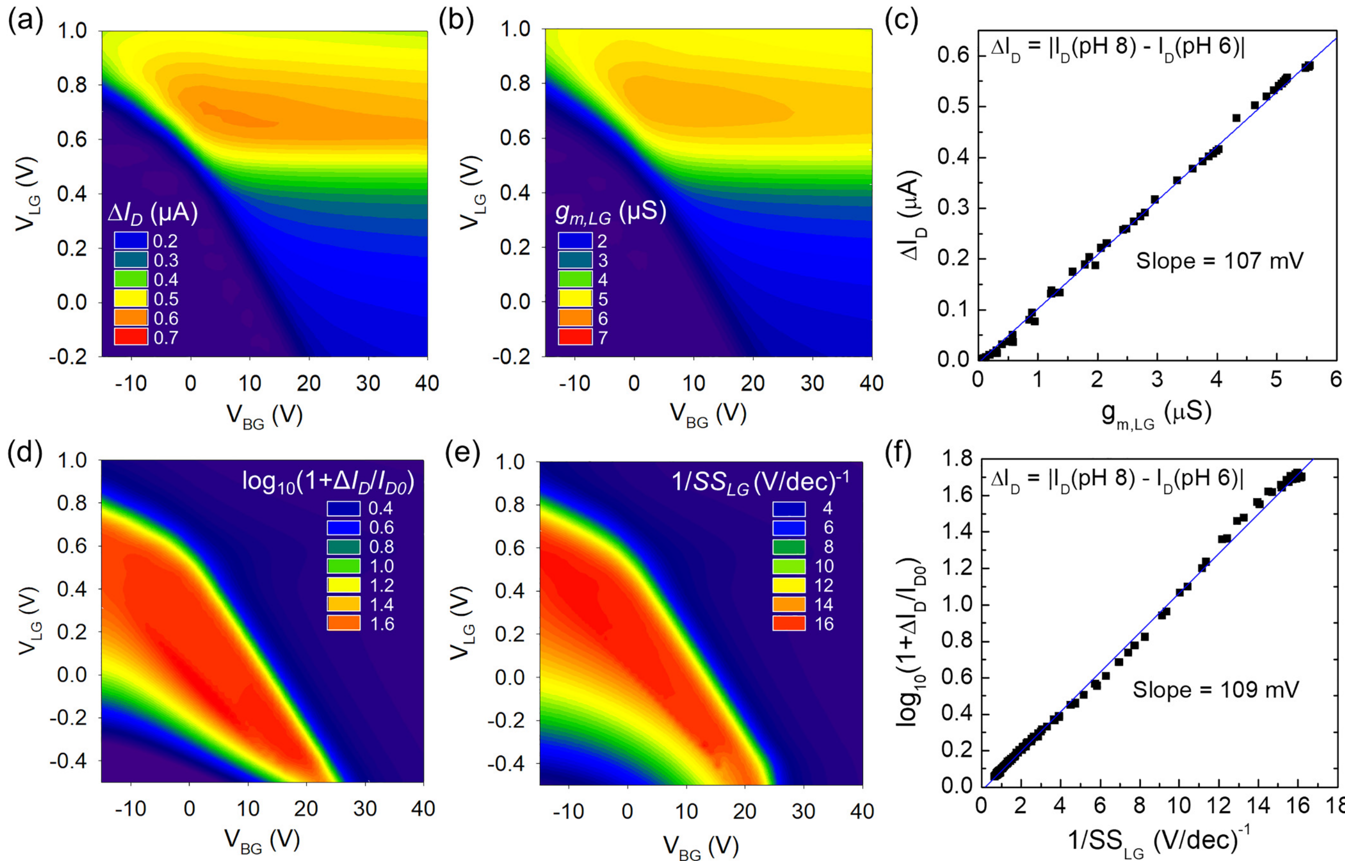

FIG. 4. (a) and (b) Two-dimensional map of the change in the drain current (ΔI_D) from pH 6 to pH 8 and transconductance measured by the liquid gate ($g_{m,LG}$) at pH 7 as a function of liquid-gate voltage (V_{LG}) and bottom-gate voltage (V_{BG}). (c) ΔI_D vs $g_{m,LG}$, showing a linear relationship with a slope of 107 mV. (d) and (e) Two-dimensional map of the normalized change in the drain current ($\Delta I_D/I_{D0}$) from pH 6 to pH 8 and subthreshold slope measured by the liquid gate (SS_{LG}) at pH 7 as a function of liquid-gate voltage (V_{LG}) and bottom-gate voltage (V_{BG}). (f) $\log_{10}(1 + \Delta I_D/I_{D0})$ vs $1/SS_{LG}$, showing a linear relationship with a slope of 109 mV. Note that ΔI_D and $\Delta I_D/I_{D0}$ are characterized from the subthreshold to the linear regime for various ranges of V_{LG} and V_{BG}. Note that the BOX thickness is 300 nm.

Published under license by AIP Publishing.

The relation between the current change (ΔI_D) and the transconductance measured by the bottom gate ($g_{m,BG} = dI_D/dV_{BG}$) is discussed in the supplementary material.

Another widely used sensing parameter is the normalized current change ($\Delta I_D/I_{D0}$), where I_{D0} represents the initial drain current. As shown in Fig. 4(d), the normalized current change of the dual-gate FET caused by the pH change from 6 to 8 increases as the voltages applied to the liquid and bottom gates decreases. This conversion of the operation conditions from the linear regime to the subthreshold regime enhances the normalized current change ($\Delta I_D/I_{D0}$), although the absolute current change (ΔI_D) is much lowered, as shown in Fig. 4(a). In the subthreshold regime, the electron carriers in the channel respond exponentially to the gate potential, and thus the current signal is increased.[39,40] The relationship between the drain current and gate voltage in the subthreshold regime can be represented with a device parameter called the subthreshold slope, which is defined as $dV_G/d\log(I_D)$. Figure 4(e) shows a two-dimensional map of the reciprocal of the subthreshold slopes measured with the liquid gate, which has a similar trend as the normalized current change shown in Fig. 4(d). The plot of the normalized current change as a function of the reciprocal of the subthreshold slope shown in Fig. 4(f) was obtained from the pairs $[\log_{10}(1 + \Delta I_D/I_{D0}),\ 1/SS_{LG}]$, where $\log_{10}(1 + \Delta I_D/I_{D0})$ and $1/SS_{LG}$ are the values at each (V_{LG}, V_{BG}) in Figs. 4(d) and 4(e), respectively. The linear dependence shown in Fig. 4(f) confirms that a direct relation exists between the normalized current change and the subthreshold slope. The slope of 109 mV between the reciprocal of the subthreshold slope and the normalized current change is similar to the value calculated from the pH responsivity in Fig. 3(f) and pH difference as 52 mV/pH × pH 2 = 104 mV. This result indicates that the normalized current change induced by the pH change is related to the potential change at the insulator/electrolyte interface. From the results in Fig. 4(f), the normalized current signal ($\Delta I_D/I_{D0}$) can be written as $\log_{10}(1 + \Delta I_D/I_{D0}) = \Delta V_{T,LG}/SS_{LG}$, where $\Delta V_{T,LG}$ is the pH-induced change in the potential at the liquid-gate side (Table I). Steep-slope devices, which have a lower subthreshold slope value than conventional devices, are suitable for biosensing to generate a higher signal for the normalized current change.[41,42] The relation between the normalized current change ($\Delta I_D/I_{D0}$) and the subthreshold slope measured by the bottom gate $[SS_{BG} = dV_{BG}/d\log(I_D)]$ is discussed in the supplementary material.

We confirmed our theory that the voltage signal (ΔV_{BG}), current signal (ΔI), and normalized current signal ($\Delta I_D/I_{D0}$) are related to the

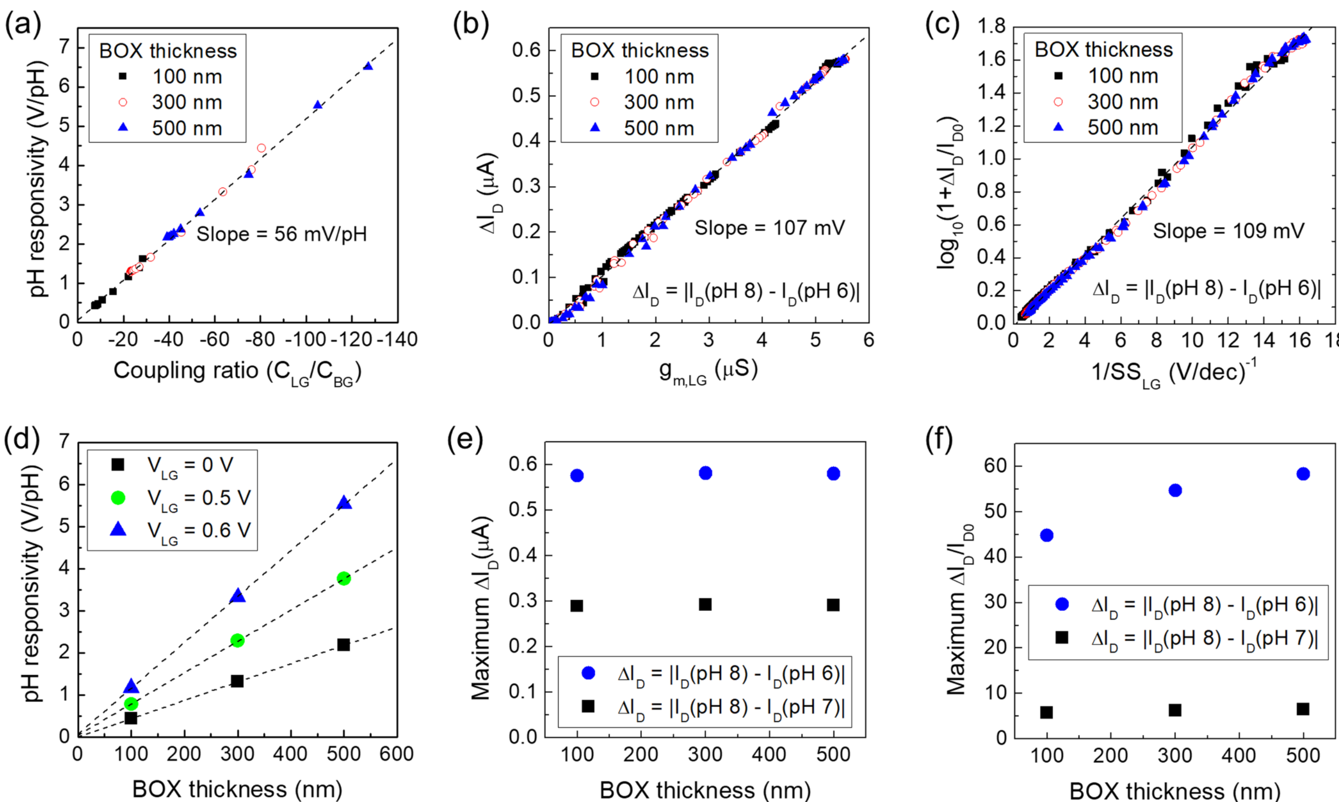

FIG. 5. (a) pH responsivity vs coupling ratio, (b) current change vs transconductance, and (c) normalized current change vs subthreshold slope in various BOX thicknesses, which show that each sensing parameter vs the corresponding electrical parameter follows a universal curve independent of the BOX thickness. Dependence of the BOX thickness on (d) pH responsivity, (e) maximum current change, and (f) maximum normalized current change.

Published under license by AIP Publishing.

capacitive coupling ratio (C_{LG}/C_{BG}), transconductance ($g_{m,LG}$), and subthreshold swing (SS_{LG}), respectively, by using an analysis with various operation conditions. As shown in Figs. 5(a)–5(c), the data obtained from various BOX thicknesses are plotted into one single line of a universal curve between the sensing parameter and its corresponding electrical parameter. The result that the signal is related to a certain electrical parameter provides an insight into the design of highly sensitive dual-gate FET-based biosensors.

Figure 5(d) shows that the pH responsivity can be easily increased with the BOX thickness, which increases the capacitive coupling ratio, C_{LG}/C_{BG}. As the BOX thickness is increased, the channel moves farther from the bottom gate. This reduces C_{BG} but keeps C_{LG} constant, which results in a high coupling ratio. In a dual-gate structure, when the BOX thickness is thicker than the thickness of the top-gate dielectric, the pH responsivity can be beyond the Nernst limit (60 mV/pH). In contrast, the maximum change in the current caused by the pH difference is not greatly affected by the BOX thickness [Fig. 5(e)]. As we discussed earlier, the current change is directly related to the transconductance instead of the coupling ratio. Because the maximum transconductance is not changed by the BOX thickness, the current signal is not improved by the modulation of the BOX thickness. Similarly, the normalized current change negligibly increases with the BOX thickness because of the same subthreshold swing [Fig. 5(f)]. Our results can explain the behavior of dual-gate FET-based pH sensors commonly observed in previous works in that the voltage signal and current signal are not enhanced simultaneously (Fig. S6 in the supplementary material).

CONCLUSIONS

In conclusion, we investigated the working mechanism of dual-gate FET-based biosensors and the origin of the signal amplification related to each electrical parameter. We confirmed that the pH signal sensed at the liquid-gate side is amplified as the voltage signal of the bottom gate by the capacitive coupling ratio between the liquid and bottom gates, which was explained via the analytical theory in the previous work.[26] The pH signal at the liquid-gate side is also transduced into a current change proportional to the transconductance; thus, a high signal can be obtained in the linear regime where the transconductance is at a maximum. If the normalized current change is used as a sensing metric, the signal is inversely proportional to the subthreshold swing and the sensitivity is maximized in the subthreshold regime. Each sensing metric measured from different structure parameters and operation conditions follows a universal curve as a function of the electrical parameter related to each sensing metric. This result implies that the sensitivity can be easily improved such that a value with the corresponding electrical parameter is maximized with the device geometry and operation condition. This study will provide a useful guideline for the future design of highly sensitive dual-gate FET-based biosensors.

METHODS

TCAD simulation

An ionic solution was modeled as an intrinsic semiconductor in a TCAD simulation using the Synopsys Sentaurus tool[43] because the properties of the electrolytes in the solution are similar to the intrinsic carriers of the semiconductor.[44] They can be expressed as the Poisson equation and the Boltzmann distribution.[45,46] To describe the ionic solution as the intrinsic semiconductor, the intrinsic carrier density (n_i) was calculated as $n_i = M_{\text{eff}} N_A/10^3$, where M_{eff} is the effective ionic concentration, N_A is Avogadro's number ($6.022 \times 10^{23}\ \text{mol}^{-1}$), and the value is adjusted using the unit of volume (cm^{-3}). The M_{eff} value was obtained by considering the number of ions having more than two valences as $M_{\text{eff}} = \frac{1}{2}\sum c_i z_i^2$, where i, c_i, and z_i indicate the number of ions in the ionic solution, the concentration of the ith ion, and the valence of the ith ion, respectively. The M_{eff} value for 0.1× phosphate-buffered saline (PBS) used in this study is 17.15 mM. Then, the n_i value of 1.03×10^{19} is updated in the simulation.

A SiO_2 layer with a thickness of 3 nm was formed on the Si channel to serve as the pH-sensitive layer (Fig. S1 in the supplementary material). A Stern layer with a 0.3-nm thickness was inserted on the SiO_2 layer to model the electric double layer (EDL) by considering the capacitance of the Stern layer ($\sim 20\ \mu\text{F/cm}^2$) and relative permittivity of the water (6.777).[2,45] The values of surface charge densities (σ_o) on the SiO_2 layer for pH values from 2 to 9 were calculated using SBM and EDL. We set a point-of-zero charge of the SiO_2 surface as 2.0, and the calculated σ_o for a pH level larger than pH 2 has a negative value. The values of σ_o for pH values from 2 to 9 were 0, -1.51×10^{-8}, -1.11×10^{-7}, -4.13×10^{-7}, -8.93×10^{-7}, -1.49×10^{-6}, -2.16×10^{-6}, and $-2.91 \times 10^{-6}\ \text{C/cm}^2$, respectively.

SUPPLEMENTARY MATERIAL

See the supplementary material for the TCAD simulation structure, effect of bottom-gate voltage on pH responsivity sensed by the liquid gate, analytical equations for the pH responsivity of dual-gate FETs, relation between current change and transconductance measured by bottom gate, relation between normalized current change and subthreshold slope measured by bottom gate, and comparison between voltage signal and normalized current signal in dual-gate FET-based pH sensors.

AUTHORS' CONTRIBUTIONS

J.-H.A. and B.C. contributed equally to this work.

ACKNOWLEDGMENTS

This work was supported by the National Research Foundation of Korea (NRF) grant funded by the Korea Government (MSIT) (No. 2020R1F1A1068242). J.-H.A. was partially supported by the Basic Science Research Program through the National Research Foundation of Korea (NRF) funded by the Ministry of Education (No. 2018R1A6A1A03025242). This work was supported by the National Research Foundation (NRF) of Korea under Grant Nos. 2016R1A5A1012966 and 2019R1A2B5B01069988 and by the Future Semiconductor Device Technology Development Program (Grant No. 10067739) funded by MOTIE (Ministry of Trade, Industry & Energy) and KSRC (Korea Semiconductor Research Consortium). The EDA tool was supported by the IC Design Education Center (IDEC), Korea.

Published under license by AIP Publishing.

DATA AVAILABILITY

The data that support the findings of this study are available within the article and its supplementary material.

REFERENCES

[1]Y. Cui, Q. Wei, H. Park, and C. M. Lieber, Science **293**, 1289 (2001).
[2]S. Chen, J. G. Bomer, E. T. Carlen, and A. van den Berg, Nano Lett. **11**, 2334 (2011).
[3]J.-H. Ahn, J.-Y. Kim, M.-L. Seol, D. J. Baek, Z. Guo, C.-H. Kim, S.-J. Choi, and Y.-K. Choi, Appl. Phys. Lett. **102**, 083701 (2013).
[4]D. Rani, V. Pachauri, A. Mueller, X. T. Vu, T. C. Nguyen, and S. Ingebrandt, ACS Omega **1**, 84 (2016).
[5]E. Stern, J. F. Klemic, D. A. Routenberg, P. N. Wyrembak, D. B. Turner-Evans, A. D. Hamilton, D. A. LaVan, T. M. Fahmy, and M. A. Reed, Nature **445**, 519 (2007).
[6]J.-H. Ahn, S.-J. Choi, J.-W. Han, T. J. Park, S. Y. Lee, and Y.-K. Choi, Nano Lett. **10**, 2934 (2010).
[7]Y. Zhang, R. Chen, L. Xu, Y. Ning, S. Xie, and G.-J. Zhang, Anal. Sci. **31**, 73 (2015).
[8]J.-I. Hahm and C. M. Lieber, Nano Lett. **4**, 51 (2004).
[9]J. Ping, R. Vishnubhotla, A. Vrudhula, and A. T. C. Johnson, ACS Nano **10**, 8700 (2016).
[10]A. Offenhäusser, C. Sprössler, M. Matsuzawa, and W. Knoll, Biosens. Bioelectron. **12**, 819 (1997).
[11]M. Lehmann, W. Baumann, M. Brischwein, H.-J. Gahle, I. Freund, R. Ehret, S. Drechsler, H. Palzer, M. Kleintges, and U. Sieben, Biosens. Bioelectron. **16**, 195 (2001).
[12]B. Tian, T. Cohen-Karni, Q. Qing, X. Duan, P. Xie, and C. M. Lieber, Science **329**, 830 (2010).
[13]M. J. Spijkman, J. J. Brondijk, T. C. Geuns, E. C. P. Smits, T. Cramer, F. Zerbetto, P. Stoliar, F. Biscarini, P. W. Blom, and D. M. de Leeuw, Adv. Funct. Mater. **20**, 898 (2010).
[14]O. Knopfmacher, A. Tarasov, W. Fu, M. Wipf, B. Niesen, M. Calame, and C. Schonenberger, Nano Lett. **10**, 2268 (2010).
[15]M. Spijkman, E. C. P. Smits, J. Cillessen, F. M. Biscarini, P. W. M. Blom, and D. M. De Leeuw, Appl. Phys. Lett. **98**, 043502 (2011).
[16]J. Go, P. R. Nair, B. Reddy, B. Dorvel, R. Bashir, and M. A. Alam, in *56th IEEE International Electron Device Meeting (IEDM), San Francisco, USA, 6–8 December 2010* (IEEE, 2010), pp. 202–205.
[17]J. Go, P. R. Nair, B. Reddy, Jr., B. Dorvel, R. Bashir, and M. A. Alam, ACS Nano **6**, 5972 (2012).
[18]H.-J. Jang and W.-J. Cho, Appl. Phys. Lett. **100**, 073701 (2012).
[19]H.-J. Jang and W.-J. Cho, Sci. Rep. **4**, 5284 (2015).
[20]C. Duarte-Guevara, F.-L. Lai, C.-W. Cheng, B. Reddy, Jr., E. Salm, V. Swaminathan, Y.-K. Tsui, H. C. Tuan, A. Kalnitsky, and Y.-S. Liu, Anal. Chem. **86**, 8359 (2014).
[21]N. Kumar, J. Kumar, and S. Panda, IEEE Electron Device Lett. **37**, 500 (2016).
[22]H.-K. Lim and J. G. Fossum, IEEE Trans. Electron Devices **30**, 1244 (1983).
[23]J. P. Denton and G. W. Neudeck, IEEE Electron Device Lett. **17**, 509 (1996).
[24]I. Y. Yang, C. Vieri, A. Chandrakasan, and D. A. Antoniadis, IEEE Trans. Electron Devices **44**, 822 (1997).
[25]M. Masahara, Y. Liu, K. Sakamoto, K. Endo, T. Matsukawa, K. Ishii, T. Sekigawa, H. Yamauchi, H. Tanoue, S. Kanemaru, H. Koike, and E. Suzuki, IEEE Trans. Electron Devices **52**, 2046 (2005).
[26]J. Go, P. R. Nair, and M. A. Alam, J. Appl. Phys. **112**, 034516 (2012).
[27]P. R. Nair and M. A. Alam, IEEE Trans. Electron Devices **54**, 3400 (2007).
[28]S. Rigante, P. Scarbolo, M. Wipf, R. L. Stoop, K. Bedner, E. Buitrago, A. Bazigos, D. Bouvet, M. Calame, and C. Schönenberger, ACS Nano **9**, 4872 (2015).
[29]K. Sun, I. Zeimpekis, C. Hu, N. M. J. Ditshego, O. Thomas, M. R. R. de Planque, H. M. H. Chong, H. Morgan, and P. Ashburn, Nanotechnology **27**, 285501 (2016).
[30]B. Choi, J. Lee, J. Yoon, J.-H. Ahn, T. J. Park, D. M. Kim, D. H. Kim, and S.-J. Choi, IEEE Trans. Electron Devices **62**, 1072 (2015).
[31]K. Besteman, J.-O. Lee, F. G. M. Wiertz, H. A. Heering, and C. Dekker, Nano Lett. **3**, 727 (2003).
[32]B. L. Allen, P. D. Kichambare, and A. Star, Adv. Mater. **19**, 1439 (2007).
[33]X. Dong, Y. Shi, W. Huang, P. Chen, and L. J. Li, Adv. Mater. **22**, 1649 (2010).
[34]J. Kim, Y. S. Rim, H. Chen, H. H. Cao, N. Nakatsuka, H. L. Hinton, C. Zhao, A. M. Andrews, Y. Yang, and P. S. Weiss, ACS Nano **9**, 4572 (2015).
[35]D. Sarkar, W. Liu, X. Xie, A. C. Anselmo, S. Mitragotri, and K. Banerjee, ACS Nano **8**, 3992 (2014).
[36]R. A. Chapman, P. G. Fernandes, O. Seitz, H. J. Stiegler, H.-C. Wen, Y. J. Chabal, and E. M. Vogel, IEEE Trans. Electron Devices **58**, 1752 (2011).
[37]I. Zeimpekis, K. Sun, C. Hu, N. M. J. Ditshego, O. Thomas, M. R. R. de Planque, H. M. H. Chong, H. Morgan, and P. Ashburn, Nanotechnology **27**, 165502 (2016).
[38]S. M. Sze and K. K. Ng, *Physics of Semiconductor Devices* (John Wiley & Sons, 2006).
[39]X. P. Gao, G. Zheng, and C. M. Lieber, Nano Lett. **10**, 547 (2010).
[40]J.-H. Ahn, J. Yun, Y.-K. Choi, and I. Park, Appl. Phys. Lett. **104**, 013508 (2014).
[41]D.-I. Moon, M. Peycelon, J.-Y. Kim, J.-H. Ahn, T. Jung Park, and Y.-K. Choi, Appl. Phys. Lett. **102**, 043701 (2013).
[42]M. Si, C.-J. Su, C. Jiang, N. J. Conrad, H. Zhou, K. D. Maize, G. Qiu, C.-T. Wu, A. Shakouri, and M. A. Alam, Nat. Nanotechnol. **13**, 24 (2018).
[43]Sentaurus Device User Guide, Version 2013.03, Synopsys, Inc., Mountain View, CA, USA, 2013.
[44]I.-Y. Chung, H. Jang, J. Lee, H. Moon, S. M. Seo, and D. H. Kim, Nanotechnology **23**, 065202 (2012).
[45]P. Bergveld, R. Van Hal, and J. C. Eijkel, Biosens. Bioelectron. **10**, 405 (1995).
[46]A. Tarasov, M. Wipf, K. Bedner, J. Kurz, W. Fu, V. A. Guzenko, O. Knopfmacher, R. L. Stoop, M. Calame, and C. Schönenberger, Langmuir **28**, 9899 (2012).

Published under license by AIP Publishing.